A synchrotron x-ray liquid surface spectrometer

Mark L. Schlossman[a)]
*Department of Physics and Department of Chemistry, University of Illinois at Chicago,
845 West Taylor Street, Chicago, Illinois 60607*

Dennis Synal, Yongmin Guan, Mati Meron, and Grace Shea-McCarthy
*Center for Advanced Radiation Sources, University of Chicago, 5640 South Ellis Avenue, Chicago,
Illinois 60637*

Zhengqing Huang
*Center for Advanced Radiation Sources and James Franck Institute and Department of Chemistry,
University of Chicago, 5640 South Ellis Avenue, Chicago, Illinois 60637*

Anibal Acero
*James Franck Institute and Department of Chemistry, University of Chicago, 5640 South Ellis Avenue,
Chicago, Illinois 60637*

Scott M. Williams
*Department of Physics and Department of Chemistry, University of Illinois at Chicago,
845 West Taylor Street, Chicago, Illinois 60607*

Stuart A. Rice
*James Franck Institute and Department of Chemistry, University of Chicago, 5640 South Ellis Avenue,
Chicago, Illinois 60637*

P. James Viccaro
*Center for Advanced Radiation Sources, University of Chicago, 5640 South Ellis Avenue, Chicago,
Illinois 60637*

The design of a synchrotron x-ray liquid surface spectrometer at beamline X19C at the National Synchrotron Light Source is described. This spectrometer is capable of performing the full range of x-ray surface scattering techniques. A few examples of measurements made using this spectrometer are presented, including studies of organic monolayers on the surface of water and of the structure of strongly fluctuating oil–microemulsion interfaces. The measurements discussed illustrate the accuracy, resolution, and capabilities of the spectrometer. © *1997 American Institute of Physics.* [S0034-6748(97)00312-2]

I. INTRODUCTION

Liquid surfaces and interfaces are of scientific interest because of their use in probing and testing ideas of structure and phase behavior at interfaces and in inhomogeneous media. They are of technological importance because of the many physical, chemical, and biological processes that occur at interfaces. Although studied for many years, fundamental questions remain concerning both the longitudinal (out-of-plane) and transverse (in-plane) structure of the interface. Recently, experimental techniques such as surface sensitive x-ray and neutron scattering[1–14] and nonlinear optical methods[15,16] have allowed these interfaces to be probed on the molecular length scale. In this article, we describe a synchrotron x-ray liquid surface spectrometer recently installed at beamline X19C at the National Synchrotron Light Source at Brookhaven National Laboratory (NSLS) and mention a few recent results from this device.

The X19C liquid surface spectrometer is capable of measuring x-ray reflection, grazing-incidence diffraction and fluorescence, surface diffuse scattering, and anomalous reflection. It has the following features: (a) the capacity to use large and heavy sample chambers; (b) a sturdy design that allows for precise (and accurate) specification of the Q vector as well as enhanced sample stability (important for liquid samples); (c) simple optics, a single-crystal monochromator or multilayer, to monochromate and steer the beam; and (d) straightforward tuning of the x-ray wavelength (from 6 to 17 keV) that allows for measurement of differential anomalous reflectivity and fluorescence, and grazing incidence anomalous x-ray scattering.

To date, the experimental techniques exploited using the X19C spectrometer have included x-ray reflectivity, surface diffuse scattering, grazing-incidence diffraction, and reflection standing-wave fluorescence. These have been used to study surfactant monolayers on the water surface,[17,18] liquid metal surfaces,[19] liquid–liquid interfaces in microemulsions,[20,21] and gold colloids in polymer thin films.[22] High-resolution coherent scattering has been used to study the propagation and scattering of partially coherent x-ray beams from surfaces of patterned optics.[23]

II. SURFACE X-RAY SCATTERING TECHNIQUES AND KINEMATICS

Surface x-ray scattering has been reviewed numerous times.[24–29] Here, we mention a few aspects necessary to understand the design of a liquid surface spectrometer. The
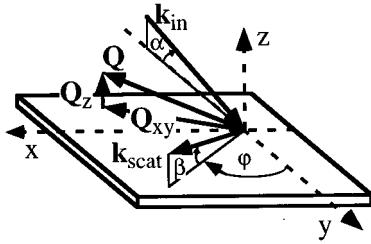
[a)]Electronic mail: schloss@tigger.cc.uic.edu

FIG. 1. Kinematics of surface x-ray scattering: $\mathbf{k}_{in}$ is the incoming wave vector, $\mathbf{k}_{scat}$ is the scattered wave vector, $\mathbf{Q}$ is the wave-vector transfer with $\mathbf{Q}_{xy} = \mathbf{Q}_x + \mathbf{Q}_y$ in the plane and $\mathbf{Q}_z$ normal to the surface.

three techniques discussed below, specular reflection, surface diffuse scattering, and grazing-incidence diffraction, are the primary techniques for studying liquid surfaces and determine most of the technical requirements for the spectrometer.

III. SPECULAR REFLECTION

The kinematics of surface scattering is illustrated in Fig. 1; note that $\alpha = 90°$ is normal to the surface. For arbitrary α, β, and φ, the three components of the wave-vector transfer of the scattered radiation, $\mathbf{Q} = \mathbf{k}_{scat} - \mathbf{k}_{in}$, are

$$Q_x = (2\pi/\lambda)\cos(\beta)\sin(\varphi),$$

$$Q_y = (2\pi/\lambda)[\cos(\beta)\cos(\varphi) - \cos(\alpha)], \qquad (1)$$

$$Q_z = (2\pi/\lambda)[\sin(\beta) + \sin(\alpha)].$$

Specular reflection occurs when $\alpha = \beta$ and $\varphi = 0$ [$Q_x = Q_y = 0$, $Q_z = (4\pi/\lambda)\sin(\alpha)$]. This reflection is usually measured at small angles where polarization effects are not important. It is convenient to consider the special case of polarization parallel to the surface. For radiation in a material of index of refraction n_1, incident on a plane surface at which the index of refraction abruptly changes to n_2, the specular reflectivity, $R_F(\alpha)$, is given by the Fresnel formula of classical optics[30]

$$R_F(\alpha) = \left| \frac{n_1 \sin\alpha - \sqrt{n_2^2 - n_1^2 \cos^2\alpha}}{n_1 \sin\alpha + \sqrt{n_2^2 - n_1^2 \cos^2\alpha}} \right|^2. \qquad (2)$$

For x-ray energies greater than the material's electronic binding energies, a simplified expression for the index of refraction, n, can be written, namely, $n = 1 - \lambda^2(\rho r_e/2\pi) + i\lambda(\mu_a/4\pi)$, where λ is the x-ray wavelength, ρ is the electron density in the material; $r_e = (e^2/mc^2) \cong 2.818$ fm is the classical electron radius, and μ_a is the x-ray linear absorption coefficient for intensity.[27]

If material 1 is air ($n_1 \cong 1$), and $n_2 < 1$ (as it is for most materials at x-ray wavelengths), there is a critical angle for x-ray total reflection, $\alpha_c = \cos^{-1}(n_2) \cong \sqrt{\rho r_e \lambda^2/\pi}$. For most materials, α_c is approximately 2–5 mrad for an x-ray wavelength of $\lambda = 0.154$ nm. If absorption is neglected, then $R_F(\alpha) = 1$ when $\alpha < \alpha_c$ and $R_F(\alpha) \approx (\alpha_c/2\alpha)^4$ when $\alpha \gg \alpha_c$. This functional form illustrates the rapid decrease in reflected intensity as the incident angle increases.

With real interfaces, for which the index of refraction profile normal to the interface changes smoothly from one bulk phase to the other, the specularly reflected intensity, $R(\alpha)$, will deviate from $R_F(\alpha)$ in a manner that allows characterization of the index of refraction profile. X-ray specular reflectivity is often interpreted in terms of the first Born approximation. The principal result is given by[24]

$$\frac{R(\alpha)}{R_F(\alpha)} \cong \left| \frac{1}{\rho_{bulk}} \int dz \, \frac{d\langle\rho(z)\rangle}{dz} \exp(iQ_z z) \right|^2, \qquad (3)$$

where $d\langle\rho(z)\rangle/dz$ is the electron density gradient averaged over the $x-y$ plane (parallel to the surface at constant z), and ρ_{bulk} is the electron density far below the surface. However, this approach neglects refraction and multiple scattering, and Eq. (3) is not accurate for $\alpha \lesssim 4\alpha_c$. Other methods of analysis are accurate at these small angles [see Eq. (21)].[26,31,32] The reflectivity can be used to measure the electron density interfacial profile, $\langle\rho(z)\rangle$, with resolution on the order of a fraction of a nanometer.

The reflectivity from simple liquid surfaces can often be characterized by a roughness, σ. For example, the reflectivity from a pure water surface for $4Q_c \lesssim Q_z \lesssim 7.5$ nm^{-1} (where Q_c is the wave-vector transfer at the critical angle for total reflection, and for water $Q_c = 0.217$ nm^{-1}) can be described by

$$\frac{R(Q_z)}{R_F(Q_z)} = \exp(-Q_z^2 \sigma^2), \qquad (4)$$

corresponding to an electron density profile in Eq. (3) given by

$$\rho(z) = \tfrac{1}{2}(\rho_l + \rho_v) + \tfrac{1}{2}(\rho_l - \rho_v)\text{erf}[z/\sigma\sqrt{2}]$$

$$\text{with } \text{erf}(z) = \frac{2}{\sqrt{\pi}} \int_0^z e^{-t^2} dt, \qquad (5)$$

where ρ_l and ρ_v are the electron density for liquid and vapor bulk phases. This interfacial profile is the prediction of the capillary wave theory by Buff, Lovett, and Stillinger.[33] Equation (4) shows that the reflectivity for a rough surface drops faster than the $(\alpha_c/2\alpha)^4$ drop-off for the smooth step-function interface.

As seen from Eq. (3), the reflectivity measures the electron density averaged over the in-plane directions, x and y, of the surface. The spatial resolution of the density profile normal to the surface is approximately $2\pi/Q_z$. Better spatial resolution can result from analysis of an experiment if there are physical or chemical constraints on the functional form of the electron density profile.

Consideration of anticipated interfacial structures provides the guideline for spectrometer design. To determine the largest Q_z necessary, consider the smallest structure that needs to be measured. In our experiments, this smallest structure occurs in the case of liquid metals. This interface has been shown to be stratified with layer spacing at the interface similar to nearest-neighbor spacing in the bulk, ~ 0.25 nm. Therefore, the reflectivity contains a peak at $Q_z \cong 25$ nm^{-1}. This sets a lower limit on the maximum Q_z needed for the spectrometer. Although higher spatial resolution is always desirable in principle, in practice, it may not

be easy to obtain for two reasons: (1) larger values of Q_z require larger spectrometer motions, which may not be practical; and 2) the surface roughness reduces the reflectivity signal. For example, a water surface has a roughness, σ, of ~ 0.27 nm resulting in a practical limitation on measurements to $Q_z \lesssim 7.5$ nm^{-1} (for x-ray wavelength $\lambda = 0.154$ nm). At larger values of Q_z, the scattering from x rays that penetrate into the bulk water overwhelms the reflectivity signal from the surface. Liquid metal surfaces are sufficiently smooth, $\sigma \cong 0.09$ nm, to allow for measurements out to $Q_z \cong 25$ nm^{-1} or higher.[19,34,35]

The requirement on the smallest accessible values of Q_z is determined by our experiments on liquid–liquid interfaces. These interfaces may have a critical wave-vector transfer for total reflection as small as $Q_c \cong 0.05$ nm^{-1}. To accurately determine the reflectivity curve, it is advantageous to be able to measure down to slightly smaller values, $Q_z \cong 0.03$ nm^{-1}. Since these systems also have a large interfacial roughness, $\sigma \cong 6$ nm or larger, which limits the maximum accessible Q_z to ~ 0.5 nm^{-1}, it is necessary to make detailed measurements over this small range of Q_z to get any information about the interface.

The desired resolution in Q_z is ~ 0.01 nm^{-1}. This is necessary to measure the reflectivity curve in the liquid–liquid systems and is also useful for measuring films as thick as 100 nm. In the latter case, oscillations due to interference between the reflection from the top and bottom layers of these films can be clearly measured only with the specified resolution.

Measurements at small Q_z also constrain the size and divergence of the x-ray beam incident on the sample. For example, liquid–liquid interfaces often have relatively small flat regions, 10–20 mm long, that are most useful for reflection measurements (a region of the sample surface is considered to be macroscopically flat if it has a slope error much smaller than the angular acceptance of the detector). At the smallest reflection angles, $\sim 2.5 \times 10^{-4}$ rad, the beam size must be ~ 10 μm at the sample for the footprint to cover only the flat region. Since the nearest distance of a beam defining slit to the center of our sample chamber is 12 cm, we use a 5 μm vertical slit gap. However, this small slit alone is inadequate because the natural vertical divergence of the beam, 1×10^{-4} rad, increases the beam size by 12 μm over the 12 cm distance. To reduce the beam divergence to 2×10^{-5} rad, two 5 μm slits placed ~ 600 mm apart on the input arm are used. These considerations set the approximate size of the input arm. Tracking the beam through these two fine slits also requires excellent angular control over the input arm.

Limitations similar to those just mentioned, for other experiments that we considered at the time of design, have set the specifications for the spectrometer as a whole and its individual components.

In addition to scanning the spectrometer over a selected range of Q_z for $Q_x = Q_y = 0$, measurements of specular reflectivity also require determination of the background scattering that must be subtracted. The finite angular resolution of the spectrometer results in a broadening of a scan along Q_y through the specular condition, as illustrated in Fig. 2.
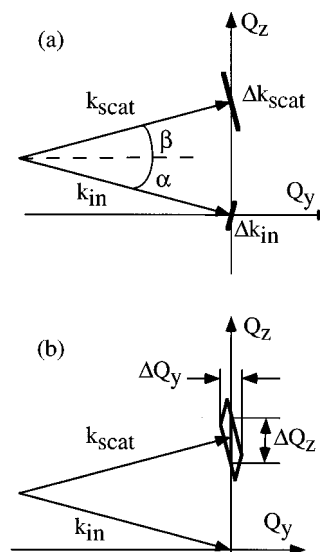

FIG. 2. Resolution considerations for specular reflectivity for which $\alpha = \beta$. (a) In the Q_y–Q_z plane the width in incoming k vectors, Δk_{in}, and the width in scattered k vectors, Δk_{scat} is shown. The widths are determined by slit sizes and the energy bandwidth. These widths may represent a square well transmission for which every k vector whose arrowhead is on the line Δk_{in} (or Δk_{scat}) is allowed; if not on the line, the k vector is forbidden. More realistically, the widths represent the width of a distribution, for example, Gaussian, of incoming and scattered wave vectors. (b) The convolution of the two resolution widths, Δk_{in} and Δk_{scat}, yield a parallelogram resolution area in the Q_y–Q_z plane. For the square well transmission, only $\mathbf{Q}$ vectors (where $\mathbf{Q} = \mathbf{k}_{scat} - \mathbf{k}_{in}$) within the parallelogram are scattered into the detector. More realistically, the parallelogram schematically represents a convolution of distributions in k_{in} and k_{scat}. The resolution area reveals an effective resolution for specular reflection in the Q_z direction, ΔQ_z, and an effective width in the Q_y direction, ΔQ_y. This shows that for a chosen angular setting of the spectrometer, specular reflection from a range of Q_z, ΔQ_z, is received by the detector. Also, to measure background scattering that does not include a component of the specular reflection, it is necessary to tune away from the specular condition by a width, $\Delta Q_y/2$, in the Q_y direction.

The background for reflectivity measurements is often measured by offsetting the spectrometer far enough in Q_y to be several resolution widths away from the specular condition. Since $\Delta Q_y = \sin \alpha (\Delta k_{in} + \Delta k_{scat}) \cong \alpha (\Delta k_{in} + \Delta k_{scat})$, for small α, it is possible to maintain the same number of resolution widths as a function of the incident angle by scanning along a line that connects $(Q_x = 0, Q_y = Q_{z,1}/a, Q_z = Q_{z,1})$ to $(0, Q_{z,2}/a, Q_{z,2})$ where a is selected such that the position $(0, Q_z/a, Q_z)$ is a chosen number of resolution widths away from the specular condition (a is determined experimentally by scanning Q_y at a fixed Q_z). Alternatively, the background can be measured by scanning along Q_z at a fixed offset in Q_y. However, this latter procedure does not maintain the same relative distance from the peak as a function of Q_z.

The x-ray absorption length, μ_a^{-1}, at 8 keV ($\lambda \cong 0.15$ nm) is approximately 1 mm in water and in most organic fluids. Since $\mu_a \propto (\text{Energy})^{-3}$, use of high-energy x rays (such as 15 keV) greatly reduces the absorption, allowing the x rays to penetrate further into the bulk liquid. Higher energies are very useful when bulk liquid needs to be penetrated to probe a buried interface, as occurs in our studies of liquid–liquid interfaces.

Although specular reflection is the dominant scattering process in the direction of $\beta = \alpha$ and $\varphi = 0$, at angles $\beta \neq \alpha$ and $\varphi \neq 0$, far enough away from the specular reflection condition, scattering from the bulk liquid is dominant. By simultaneously measuring the angular dependence of the specular reflectivity and bulk scattering, it is possible to monitor the structure of the bulk liquid in the same experiment in which the surface structure is studied.

IV. SURFACE DIFFUSE SCATTERING

Tuning off the condition for specular reflection results in a nonzero in-plane component of the wave-vector transfer, $\mathbf{Q}_{xy} \equiv (Q_x, Q_y)$ (this scattering is referred to as surface diffuse scattering). For small angle scattering off the specular condition, if $|\alpha - \beta| \ll \alpha \ll 1$ and $\varphi = 0$, then $Q_z \cong (4\pi/\lambda)\alpha$, $Q_x = 0$ and $Q_y \cong (\pi/\lambda)(\alpha^2 - \beta^2) \cong (Q_z/2)(\alpha - \beta)$, resulting in values of Q_y as small as $10^{-7}(2\pi/\lambda)$. This allows for measurements that are sensitive to long-wavelength structures at the interface, such as long-wavelength capillary waves. For example, if $\alpha = 0.5°$, $\alpha - \beta \cong 0.1°$, and $\lambda = 0.15$ nm, then $2\pi/Q_y \cong 10$ μm, comparable to the smallest length scales usually probed in scattering by visible light; however, with x rays, the measurements can be extended to length scales that are orders of magnitude smaller.

If the surface or interface is not perfectly smooth and if the amplitude of the height fluctuations, $\zeta(x,y)$, are small in comparison with $1/Q_z$, the distorted wave Born approximation yields the following form for the differential cross section for x-ray surface diffuse scattering:[32,36–38]

$$\frac{d\sigma}{d\Omega} = r_e^2 A_{xy} |T(\alpha)|^2 |T(\beta)|^2 \int dx\, dy\, \rho^2 \langle \zeta\zeta(x,y)\rangle e^{i\mathbf{Q}_{xy}\cdot\mathbf{r}}, \tag{6}$$

where ρ is the average electron density, A_{xy} is the illuminated area of the sample, and $\langle \zeta\zeta(x,y)\rangle$ is the height–height correlation function. $T(\vartheta)$, $\vartheta = \alpha$ or β, is the Fresnel transmission coefficient for the amplitude of the total wave field at the surface, polarized perpendicularly to the plane of incidence, written as[30]

$$T(\vartheta) = \frac{2n_1 \sin\vartheta}{n_1 \sin\vartheta + [n_2^2 - n_1^2 \cos^2\vartheta]^{1/2}}. \tag{7}$$

For small angles and $n_1 = 1$, $T(\vartheta) \cong 2\vartheta/[(\vartheta + \sqrt{\vartheta^2 - \vartheta_c^2}]$, and $|T(\vartheta)|^2 \cong (2\vartheta/\vartheta_c)^2 \sqrt{R_F(\vartheta)}$. The function $|T(\alpha)|^2$, which is proportional to the square of the field, varies from 0 to 4, as α increases from 0 to α_c, and then falls to unity for $\alpha \gg \alpha_c$. The factor $T(\beta)$ appears because of a similar effect in the coupling between the surface currents and the scattered fields.[36,39–43]

The angular dependence of the two factors, $T(\alpha)$ and $T(\beta)$, enables the surface scattering to be distinguished from other diffuse scattering processes. This is particularly useful for probing the height fluctuations due to thermally excited capillary waves. In this case, the scattered intensity, I_D, is written as[37]

$$I_D = I_o \frac{(r_e\rho)^2}{\alpha\Delta\alpha} \frac{k_B T}{\gamma} \int_{(\alpha-\Delta\alpha/2)}^{(\alpha+\Delta\alpha/2)} d\alpha \int_{(-\Delta\varphi/2)}^{(\Delta\varphi/2)} d\varphi$$
$$\times \int_{(\beta-\Delta\beta/2)}^{(\beta+\Delta\beta/2)} d\beta \frac{|T(\alpha)|^2 |T(\beta)|^2}{q^2 + k_g^2}, \tag{8}$$

where I_o is the total incident flux, γ is the measured interfacial tension, and $k_g^2 = \Delta\rho_m g/\gamma$ where $\Delta\rho_m$ is the *mass* density difference between the two bulk phases, g is the gravitational acceleration, and $\Delta\alpha$, $\Delta\beta$, and $\Delta\varphi$ are the widths of the distributions of the respective angles, where φ is an in-plane azimuthal angle.

These measurements are made either by scanning in Q_y or by fixing the incident angle, α, and scanning the scattering angle, β, in the plane of incidence. For the more demanding studies of liquid–liquid interfaces, the required resolution is $\sim 10^{-6}$ nm^{-1} in Q_y or 0.001° in angle. Scanning Q_y may also require a sample motion accurate to 1 μm for small samples, so the beam footprint stays on the flat area of the sample. For this reason, it is often simpler to scan the scattering angle with a fixed incident angle. The other spectrometer requirements for surface diffuse scattering measurements are similar to those for reflectivity measurements.

V. GRAZING INCIDENCE DIFFRACTION

Scattering from the surface can also dominate when, for $\alpha \lesssim \alpha_c$, the incident wave is totally reflected.[44] Neglecting absorption, the incident intensity penetrates the surface as an evanescent wave, which falls off as $\exp(-z/\Lambda_i)$, where $\Lambda_i \cong [(4\pi/\lambda)\sqrt{\alpha_c^2 - \alpha^2}]^{-1}$. For $\alpha_c \cong 0.2°$, $\alpha = 0.8\alpha_c$, and $\lambda = 0.15$ nm, the intensity is reduced to $1/e$ of its initial value in approximately 5 nm. For this value of α and almost any value of $\beta \lesssim 10°$, scattering in the φ direction at $Q_{xy} \equiv \sqrt{Q_x^2 + Q_y^2} \equiv (4\pi/\lambda)\sin(\varphi/2)$ will probe structure parallel to the surface and within approximately 10 nm of the interface. This experimental geometry can be used, for example, to investigate the in-plane structure of molecular monolayers at the liquid–vapor interface.

For a monolayer of point particles at the liquid–vapor interface, the distorted wave Born approximation yields the following generalization of Eq. (6):[36–38]

$$\frac{d\sigma}{d\Omega} = r_e^2 A_{xy} |T(\alpha)|^2 |T(\beta)|^2 \int dx\, dy \langle \rho_s \rho_s(x,y)\rangle e^{i\mathbf{Q}_{xy}\cdot\mathbf{r}}, \tag{9}$$

where $\rho_s(x,y)$ describes the surface electron density of the point particles, that is $[\rho(x,y,z) - \langle\rho(z)\rangle] \cong \rho_s(x,y)\delta(z)$, and A_{xy} is the illuminated area of the sample. If the particles form a two-dimensional ordered phase, the evanescent wave will diffract from the in-plane order when the in-plane transferred momentum Q_{xy} corresponds to an in-plane reciprocal lattice vector $\mathbf{G}_{xy}$, regardless of the value of Q_z. As a consequence, there are Bragg rods of scattering for surface order (instead of Laue spots as for bulk diffraction).[45] For point particles, the intensity along the Bragg rod will be determined only by the classical surface field enhancement, $T(\alpha)$ and $T(\beta)$, described previously, and by polarization effects. If the particles in the monolayer are molecules, then the in-

TABLE I. Spectrometer and beamline motors.

Name (mnemonic)	Purpose	Hardware	Step size
Slit 1 vertical (s1v)	Vertical beam size before mirror	NSLS design	N/A
Slit 2 horizontal (s1h)	Horizontal beam size before mirror	NSLS design	N/A
Mirror bend (mirb)	Adjusts mirror focus vertically	Custom	4.5 μm
Mirror jack 1 (mirj1)	Vertical mirror motion	Custom	3.5 μm
Mirror jack 2 (mirj2)	Vertical mirror motion	Custom	3.5 μm
Mirror jack 3 (mirj3)	Vertical mirror motion	Custom	3.5 μm
Mirror translation 1 (mirt1)	Horizontal mirror motion	Custom	4.0 μm
Mirror translation 2 (mirt2)	Horizontal mirror motion	Custom	4.0 μm
Slit 2 outer (s2o)	Vertical beam size after mirror	Custom	4.0 μm
Slit 2 inner (s2i)	Vertical beam size after mirror	Custom	4.0 μm
Slit 2 left (s2l)	Horizontal beam size after mirror	Custom	6.3 μm
Slit 2 right (s2r)	Horizontal beam size after mirror	Custom	4.0 μm
Monochromator translation (monot)	Adjusts position of monochromator within the 3-circle	Custom	4.0 μm
Theta (th)	Θ, 3-circle theta stage for monochromator alignment	Huber 410	$5\times10^{-3\circ}$
Chi (chi)	χ, beam steering	Huber 511.1	$5\times10^{-4\circ}$
Phi (phi)	Φ-stage sets θ_B, Bragg angle, for beam energy	Huber 511.1	$5\times10^{-4\circ}$
Two theta (tth)	2θ, spectrometer rotation	Huber 440	$5\times10^{-4\circ}$
Input height (ih)	Input arm vertical translation	Anorad 7-6 (100 mm travel)	1.3 μm
Input rotation (ir)	α, input arm rotation	Huber 414	$5\times10^{-4\circ}$
Sample height (sh)	Sample vertical translation	Custom	1.3 μm
Sample theta (sth)	Sample rotation	Franke PDM400M	$5\times10^{-3\circ}$
Detector theta (dth)	φ, detector rotation about sample center	Franke PDM400M	$5\times10^{-3\circ}$
Output rotation (or)	β, output arm rotation	Franke PDM175M	$5\times10^{-4\circ}$
Output height (oh)	Output arm vertical translation	Anorad 7-10 (200 mm travel)	1.3 μm
Spectrometer translation (yt)	Translates entire spectrometer and monochromator tank transverse (horizontal) to the beam	Custom	3.2 μm
Hutch slit motors (s♯b, s♯t s♯l, or s♯r)	4-jaw slit motions in hutch, ♯ identifies slit; t, b, l, or r identifies jaw (top, bottom, left, right)	Huber slits	0.6 μm or 1.2 μm
Hutch absorber (habs)	Absorber wheel in hutch	Custom	N/A
Beamline absorber (babs)	Absorber foil in beamline	Custom	N/A

tensity, $I(Q_z)$, along the Bragg rod is modulated by the molecular structure factor normal to the surface, $F(\mathbf{G}_{xy}, Q_z)$, and is represented as

$$I(Q_z) \propto |T(\alpha)|^2 |F(\mathbf{G}_{xy}, Q_z)|^2 |T(\beta)|^2. \qquad (10)$$

For monolayers of long molecules that exhibit ordering of the molecular tilts, the factor $F(\mathbf{G}_{xy}, Q_z)$ is a function of both the molecular tilt and the intrinsic molecular structure factor. The intensity distribution along the Bragg rod provides information analogous to that contained in reflectivity measurements, but only for the ordered part of the monolayer.

Scans in φ using the detector theta rotation stage (''dth'') are used to determine the locations of the Bragg rods in Q_{xy}, thereby determining the reciprocal lattice of the in-plane order (see Table I). Due to the weak scattering from the ordered structures of Langmuir monolayers, a Soller slit with in-plane angular resolution of 3×10^{-3} rad is used to maximize the signal.[8] Structure along the Bragg rods is usu-

ally measured at X19C with a gas ionization position sensitive wire detector (Ordela, 200 mm long active wire region).[46] A single measurement with this detector scans a range in Q_z of ~ 1 Å^{-1} (at an x-ray energy of 8 keV). The range in Q_z may be essentially doubled by translating the detector with the ''oh'' stage (see Table I). The minimum width of a peak along the Bragg rod is approximately the inverse of the monolayer thickness, typically, 1/20 Å^{-1}. The resolution of the linear detector in Q_z is $\sim 3\times10^{-4}$ rad, far exceeding that necessary to measure the peak widths. This allows many (typically, 100–200) adjacent detector channels to be summed, improving the signal-to-background ratio.

VI. DESIGN

A. X19C beamline

The X19C beamline delivers radiation in the energy range from 6 to 17 keV. The beam is focused in the vertical and horizontal by a cylindrically cut mirror that is mechani-

Monochromator	Energy (keV)	Flux (photons/s)
Si(111)	8	3×10^{11}
Si(111)	15	2×10^{10}
Multilayer (17.5 Å 2d spacing)	8	$>7\times10^{12}$
Multilayer (17.5 Å 2d spacing)	15	6×10^{11}

cally bent. The measured beam spot size (full width at half-maximum) near the focus in the experimental area is 0.4 mm×1 mm (vertical×horizontal). The angular divergence of the beam is 100 μrad in the vertical and 2 mrad in the horizontal. The resultant x-ray fluxes from different monochromators at two sample energies are listed in Table II.

B. Spectrometer overview

There are several different methods for experimentally achieving the kinematic conditions needed for detection of scattering from liquid surfaces.[3,5,13,47–50] Reflection and surface diffuse scattering require the use of incident angles much larger than the critical angle for reflection from a mirror and, therefore, a monochromator crystal is used to steer the beam downward. Our spectrometer consists of the following major components: (1) a flat single-crystal monochromator to select the wavelength and steer the x-ray beam downward; (2) a rotary (2θ) stage to orient the spectrometer to intercept the x-ray beam of the chosen energy; (3) slits on input and output (detector) arms to adjust the size of the beam incident on the sample and set the resolution; (4) a sample stage to adjust the vertical position of the sample as appropriate for the desired angle of incidence; and (5) an output arm and detector that can be appropriately oriented about the sample to choose both the Q vector and resolution.

The X19C spectrometer has the following features:

(i) Range in Q_z of 0.01 nm^{-1}$\leq$$Q_z$$\leq$30 nm^{-1}. Resolution in Q_z is ~0.01 nm^{-1} with a typical reproducibility of better than 0.03 nm^{-1}.

(ii) For grazing-incidence diffraction, the detector theta motion is at least $\pm$90°. The in-plane Q-space resolution is 0.07 nm^{-1} (using Soller slits) with a reproducibility of 0.015 nm^{-1}.

(iii) For surface diffuse scattering, the resolution in Q_y is 10^{-5} nm^{-1} with a typical reproducibility of better than 3×10^{-5} nm^{-1}.

(iv) The capacity to use large and heavy sample chambers, as required for high-vacuum experiments. Sample chambers of 100 kg (with a center of mass ~0.3 m from the bottom) that can fit on a 0.6 m×0.75 m table are easily accommodated.

(v) Simple wavelength tuning from 6 to 17 keV, allowing for measurement of differential anomalous reflectivity and fluorescence, and grazing incidence anomalous x-ray scattering (these techniques have yet to be used).

(vi) Simple spectrometer optics consisting of a single, flat monochromator. The monochromator tank is designed for easy access to all components, thereby allowing
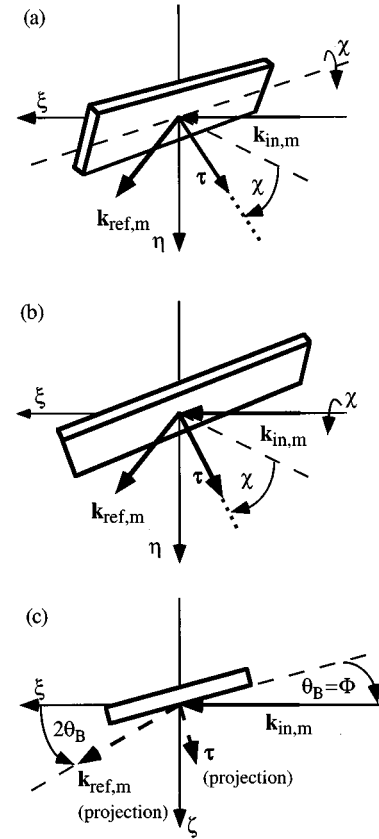

FIG. 3. The axis ζ is out of the paper for parts (a) and (b). The dashed lines in (a) and (b) are in the ξ–ζ plane. (a) Kinematics for beam steering when the monochromator is rotated about its long axis. (b) Kinematics for beam steering when the monochromator is rotated about an axis collinear with the incoming x-ray beam. (c) Projection of kinematics in part (b) onto the ξ–ζ plane. The axis η is into the paper.

for the easy replacement of monochromators for particular experiments. For example, experiments which can be carried out with lower resolution but need higher flux will benefit from the use of multilayer monochromators. X19C currently has both silicon(111) and multilayer monochromators of d spacing equal to 1.75 and 1.2 nm,[51] see Table II.

(vii) The spectrometer is permanently installed in the X19C hutch. This reduces the setup time for an experiment in comparison with portable spectrometers.

C. Steering crystal monochromator

A single reflection off a flat monochromator crystal or multilayer is used to select the x-ray energy and to steer the x-ray beam from its initial direction of approximately 9 mrad from the horizontal to the desired incident reflection angle on the sample. Two useful rotation geometries are available for this beam steering. In the first, the monochromator is rotated about an axis along the length of the monochromator and in the plane of the monochromator. The monochromatic beam is then steered in a plane at a fixed 2θ [see Fig. 3(a)] with a small change in x-ray energy as a function of the incident angle on the sample. This geometry has been described in detail by Pershan et $al.$[6] and can be used when the x rays

incident upon the monochromator have large enough bandwidth to accommodate this energy variation and when the experimental technique can permit it. An alternative geometry uses a rotation of the monochromator about the axis collinear with the incoming beam [see Fig. 3(b)]. This has the advantage that the x-ray energy is fixed as a function of incident angle. However, the beam is steered in a cone, demanding that the spectrometer follow the beam by varying 2θ as the angle of incidence is varied. This alternative geometry is necessary when monochromatic x rays (from a beamline monochromator, as, for example, at NSLS beamline X22B) are incident on the steering monochromator or when the experimental technique requires a fixed energy. The X19C spectrometer is capable of either geometry, though the latter is usually used and will be described in this manuscript.

At X19C, the x rays incident on the monochromator are broadband in energy with a horizontal divergence of 2 mrad and a vertical divergence of 0.1 mrad. The beam steering geometry mixes the horizontal and vertical divergence as the monochromator is rotated. This changes the shape of the beam reflected from the monochromator and is particularly noticeable when using multilayer monochromators that require large rotation angles to achieve the desired angle of incidence on the sample. Due to the large horizontal divergence, $\Delta E/E \cong 3 \times 10^{-3}$ for the Si(111) monochromator and $\Delta E/E \cong 5 \times 10^{-3}$ for the multilayer monochromator (at 8 keV), despite the much smaller natural bandwidth of the Si(111) crystal. The multilayer monochromator's bandwidth is well matched to the optics, resulting in an increase in photon flux by a factor of 25 over that from the Si(111) (Table II). When using the Si(111) crystal, we calculate that by reducing the horizontal beam divergence before the monochromator, the energy bandwidth, ΔE, can be reduced to $\sim 5-10$ eV. Reduction of ΔE to nearly this value has been recently accomplished.[52]

Here, we review the relationship between the incident wave vector, $\mathbf{k}_{\mathrm{in},m}$, onto the steering monochromator and the wave vector reflected from the monochromator, $\mathbf{k}_{\mathrm{ref},m}$. When the beam is not steered, the plane of incidence is the ξ–ζ plane, as shown in Fig. 3(c). The incident angle is the Bragg angle, θ_B. In (ξ,η,ζ) space, $\mathbf{k}_{\mathrm{in},m}=k(1,0,0)$, where $k=|\mathbf{k}_{\mathrm{in},m}|=2\pi/\lambda$, and λ is the x-ray wavelength; the reciprocal lattice vector $\boldsymbol{\tau}=\tau[-\cos(\pi/2-\theta_B),0,\sin(\pi/2-\theta_B)]$. In this case, the wavelength is the central wavelength determined by the monochromator and the incident angle. The rays drawn in Figs. 3(a)–3(c) are the central rays. The reflected wave vector is then written as

$$\mathbf{k}_{\mathrm{ref},m}=\mathbf{k}_{\mathrm{in},m}+\boldsymbol{\tau}=(k-\tau\sin(\theta_B),0,\tau\cos(\theta_B)). \tag{11}$$

The Bragg condition for diffraction (reflection, in this case) from a perfect crystal can be written as $\tau=2k\sin(\theta_B)$ leading to $\mathbf{k}_{\mathrm{ref},m}=k(\cos(2\theta_B),0,\sin(2\theta_B))$ as expected for simple Bragg reflection.

It is now easy to consider the effect of a rotation of the monochromator through an angle χ about the ξ axis, as shown in Fig. 3(b). The reciprocal lattice vector is written as

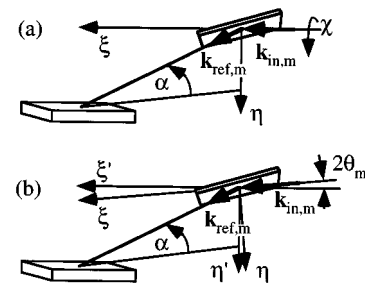$$\boldsymbol{\tau}=\tau(-\sin(\theta_B),\cos(\theta_B)\sin(\chi),\cos(\theta_B)\cos(\chi)), \tag{12}$$

FIG. 4. (a) X-ray beam steering onto sample at incident angle α. (b) As in part (a) with the inclusion of the reflection angle from the mirror, θ_m.

resulting in

$$\mathbf{k}_{\mathrm{ref},m}=k(\cos(2\theta_B),\sin(2\theta_B)\sin(\chi),\sin(2\theta_B)\cos(\chi)). \tag{13}$$

Note that the ξ component of $\mathbf{k}_{\mathrm{ref},m}$ is independent of χ indicating that $\mathbf{k}_{\mathrm{ref},m}$ rotates in a cone about the ξ axis. The spectrometer has to vary 2θ to follow $\mathbf{k}_{\mathrm{ref},m}$. By projecting $\mathbf{k}_{\mathrm{ref},m}$ into the ξ–ζ plane, as shown in Fig. 3(c), it is seen that

$$\tan(2\theta)=\frac{k_{\mathrm{ref},\zeta}}{k_{\mathrm{ref},\xi}}=\frac{\sin(2\theta_B)\cos(\chi)}{\cos(2\theta_B)}=\tan(2\theta_B)\cos(\chi). \tag{14}$$

The angle of incidence onto the sample, α, is determined by the η component of $k_{\mathrm{ref},m}$ (denoted $k_{\mathrm{ref},m,\eta}$) as

$$\sin(\alpha)=k_{\mathrm{ref},m,\eta}/k=\sin(2\theta_B)\sin(\chi), \tag{15}$$

or

$$\chi=\sin^{-1}[\sin(\alpha)/\sin(2\theta_B)], \tag{16}$$

which gives the monochromator rotation angle, χ, for a desired angle of incidence, α [see Fig. 4(a)].

At X19C, the geometry is slightly more complicated because the x-ray beam incident on the monochromator deviates from the horizontal by approximately 9 mrad, but the sample, being liquid, maintains a fixed horizontal surface determined by gravity. Figure 4(b) identifies the mirror reflection angle as $2\theta_m$ in the ξ–η plane. If we consider the ξ–η–ζ space to be attached to the steering monochromator (as used above) and a ξ'–η'–ζ' space attached to the sample, then $\mathbf{k}_{\mathrm{ref},m}$ in the primed coordinates can be written in terms of a simple rotation about the $\zeta(\equiv\zeta')$ axis. This gives

$$\begin{pmatrix} k_{\mathrm{ref},m,\xi'} \\ k_{\mathrm{ref},m,\eta'} \\ k_{\mathrm{ref},m,\zeta'} \end{pmatrix}$$
$$=k\begin{pmatrix} \cos(2\theta_B)\cos(2\theta_m)-\sin(2\theta_B)\sin(2\theta_m)\sin\chi \\ \cos(2\theta_B)\sin(2\theta_m)+\sin(2\theta_B)\cos(2\theta_m)\sin\chi \\ \sin(2\theta_B)\cos\chi \end{pmatrix}, \tag{17}$$

where the ζ' component is unchanged. As before, 2θ is determined by the projection onto the ξ'–ζ' plane and is given by
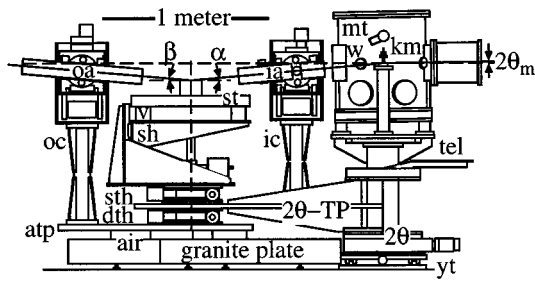
FIG. 5. Side view of liquid surface spectrometer (refer to Table I): mt, monochromator tank; km, kinematic mount (only 1 of 3 mounting places shown); tel, alignment telescope mounting plate (telescope not shown); w, monochromator tank window; ia, input arm; ic, input column; yt, horizontal motion (transverse to the beam) for the spectrometer and monochromator tank together; $2\theta_m$, twice the mirror reflection angle; 2θ TP, 2θ tie plate connecting the 2θ stage to the rest of the spectrometer; sth, sample theta (rotation); dth, detector theta (rotation); sh, sample height stage (vertical motion); vib, vibration isolation blocks; air, air bearings (total of 3); atp, air bearing tie plate connecting the three air bearings; oc, output column; and oa, output arm.

$$2\theta = \tan^{-1}\left[\frac{\tan(2\theta_B)\cos\chi}{\cos(2\theta_m) - \tan(2\theta_B)\sin(2\theta_m)\sin\chi}\right], \quad (18)$$

and α is determined by $\sin(\alpha) = k_{\mathrm{ref},m,\eta'}/k$ and is given by

$$\sin\alpha = \cos(2\theta_B)\sin(2\theta_m) + \sin(2\theta_B)\cos(2\theta_m)\sin\chi. \tag{19}$$

Use of Eq. (19) allows us to write the monochromator rotation angle, χ, in terms of the angle of incidence on the sample, α, as

$$\chi = \sin^{-1}\left[\frac{\sin\alpha - \cos(2\theta_B)\sin(2\theta_m)}{\cos(2\theta_m)\sin(2\theta_B)}\right]. \tag{20}$$

Because of the mirror reflection, $\alpha = 0$ does not correspond to $\chi = 0$.

To execute the necessary motions, the monochromator is mounted on the Φ stage of a 3-circle goniometer (i.e., a 4-circle geometry goniometer without the lowest, 2θ, stage). This custom 3-circle was assembled from Huber Model Nos. 410 and 511.1 by Blake Industries.[53,54] The Φ stage is used to set the x-ray energy by setting θ_B. The χ stage performs the χ motion described above. To align the χ axis to be collinear with the incoming beam requires rotation of the χ and Φ stages as a unit about an approximately vertical axis (the η axis). This rotation is performed by the Θ stage of the 3-circle. The alignment of the χ axis also requires a rotation about a horizontal axis normal to the beam path (defined by the x-ray direction incident upon the monochromator). This rotation is possible because the entire monochromator tank is mounted on kinematic mounts that allow for small rotations about the ζ axis through the monochromator (see Fig. 5). Deviation from perfect alignment results in changes in the x-ray energy as the beam is steered to different angles (see the Appendix).

The 2θ stage (Huber 440) is not directly attached to the 3-circle, but is displaced vertically downward by ~ 1 m. The 2θ-axis and 3-circle rotation axes are aligned by using a telescope, that rotates concentrically with the 2θ axis, to sight on
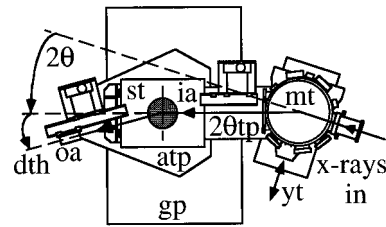

FIG. 6. Top view of liquid surface spectrometer (refer to Table I): mt, monochromator tank; yt, horizontal motion (transverse to the beam) for the spectrometer and monochromator tank together; 2θ-tp, 2θ tie plate connecting the 2θ stage to the rest of the spectrometer; dth, detector theta (rotation); atp, air bearing tie plate connecting the three air bearings; ia, input arm; and oa, output arm.

a cross hair placed at the center of the 3-circle rotation. This optical alignment is performed with the monochromator tank closed, by sighting through four windows placed 90° apart. Note that the entire 3-circle is tilted at ~ 9 mrad ($2\theta_m$) with respect to the 2θ stage. The 2θ stage rotates the rest of the spectrometer, including the sample, in a horizontal plane (see Figs. 5 and 6).

The monochromator is mounted directly on a water-cooled block mounted on a linear translation stage (''monot'') that is then mounted on the 3-circle's Φ stage. This stage is used to translate the monochromator out of the beam and replace it with a cross hair centered on the rotation axes of the 3-circle. Shining the x-ray beam on the cross hair allows the 3-circle and the rest of the spectrometer to be centered on the beam. This placement is effected by moving the entire spectrometer including the monochromator tank with a translation stage (''yt'') placed below the 2θ stage. The relative position of the center of the monochromator 3-circle with respect to the spectrometer is, therefore, undisturbed (see Figs. 5 and 6).

The steel monochromator tank is pumped down to 10^{-3} Torr, filled with helium, and then left with a small flow of helium during usage. The monochromated and steered x rays exit the tank through a large (8 cm×24 cm), flat, beryllium or kapton, window. A window cover is used when changing the pressure in the tank to ensure that there is essentially no pressure gradient across the window. To protect the beryllium window from oxidation, a thin layer (200 nm) of aluminum was deposited on the outside of the window. However, this deteriorated after exposure to the focused white beam. The beryllium window is now used with a kapton window over it and a flow of helium gas between the two windows.

D. Air bearing mechanism

When rotated by the Huber 440 2θ stage, the spectrometer is supported by three air bearing pads (0.3×0.3 m² area for each) riding on a granite plate (1.9 m×1.2 m×0.15 m). The air bearings and the truncated triangular tie plate (see Fig. 6) were engineered and manufactured by Dover Instrument Corp.[55] This bearing mechanism supports a 270 kg load centered on the sample table (including a sample chamber of 100 kg or less) and a 90 kg load from the output arm support structure that is offset by 685.8 mm from the center. The air

bearing mechanism can rotate 37° in 2θ on a radius of 1238.25 mm (distance from the monochromator to sample center) (see Fig. 6).

The mechanism serves a dual purpose by also providing the bearing mechanism for the detector rotation. When the 2θ tie plate is fixed at a specified angle and the dth stage rotates, the air bearing tie plate rotates about a vertical axis through the sample center. The dth rotation range is a minimum of $\pm 90°$ for $10° < 2\theta < 35°$. Limitations on this rotation range are due to the position of the experimental hutch wall and interference between the output column and the 2θ tie plate.

The granite plate is flat to within 2.5 μm and was leveled to better than 1×10^{-4} rad when installed. For motion in the horizontal plane, the vertical motion of a given reference point on the air bearing tie plate surface (with respect to the granite plate) does not exceed 2.5 μm over the entire excursion of the bearing mechanism.

E. Input and output arms

The input and output arms, shown schematically in Figs. 5 and 6, are centered 558.8 mm from the monochromator and 685.8 mm from the sample center, respectively. These hold Klinger rails (X-95)[56] onto which the experimenter can attach slits (e.g., motorized Huber slit assemblies), ion chambers, scintillator detectors (mounted vertically or horizontally), Soller slits, a linear detector, evacuated beam paths, or other optical elements as needed for a particular experiment. The rails are easily replaced with others of different length, and the optical components can be placed at most points along the beam path. The vertical position of the components placed on the rail is very reproducible (within a few micrometers). The input arm is oriented and positioned correctly in the beam using an Anorad 7-6 linear translation stage mounted for vertical translation (''ih'') and a Huber 414 double rotation stage (''ir'') rotating about a horizontal axis. The other rotation axis of the Huber 414 can be used to rotate a crystal into the beam. This allows the incident energy as a function of monochromator steering angle to be measured as the incident angle is varied (by using a detector on the end of the input arm).

The output arm, which normally holds a detector, is oriented and positioned in a similar fashion with a vertical translation stage (Anorad 7-10) and a rotation about a horizontal axis (Franke PDM175M rotary table). Because of the significant torque loads on both the input and output arms, additional bearing surfaces were added for both the translations and rotations.

The input and output arms and their associated motion stages are supported on the input and output columns, respectively. The input column is mounted on the 2θ tie plate connecting the 2θ stage and the detector rotation stage. The output column is mounted on the air bearing tie plate that is rotated about the sample center by the dth stage.

F. Sample table and vibration isolation

The mounting surface for sample chambers is a 0.6 $\times 0.75$ m^2 breadboard from Newport Research Corp.[56] that is

vibration isolated by a MOD-2 isolation system from JRS.[57] This system isolates the liquid surfaces from mechanically induced vibrations. It provides active-feedback vibration isolation, which maintains the absolute vertical position of the breadboard to within 1 μm (and rotations to within 2 μrad), necessary for maintaining sample alignment for the very small grazing incident angles typically used to study liquid surfaces. The sample height (''sh'') stage is a custom built vertical translation stage with 290 mm of travel and a step size of 1.3 μm. Optical encoder feedback of this stage results in a motion accuracy of ~ 3 μm, primarily limited by the mechanical creep of the stage (encoder from Heidenhain[58]). For higher precision work, small samples can be mounted on a small, accurate translation stage mounted on top of the sample breadboard.

The sample table can be rotated about its center by a Franke rotary table (PDM400M, ''sth''). Although the sample rotation may be limited by the use of large sample chambers, the table is capable of rotating 360°.

G. Electronics and computer control

The motions of the spectrometer and beamline motors as well as the electronic signals from the detectors are controlled and read by a Sun Sparcstation 2 using hardware and software that are standard in the x-ray scattering community. The software is a commercial package called SPEC (Certified Scientific Software).[59] The X19C spectrometer uses the Surf module of the SPEC software whose macrolanguage has been used to customize the software for X19C. A CAMAC interface is used for motor control (E-500 stepper motor controllers from DSP[60]) and for counting single-channel detectors such as NaI scintillators (Bicron Corp.[61]) using counting and timing electronics from Kinetic Systems (3610 Hex Counter and 3655 Timing Generator[62] and detector signal amplification electronics from Ortec (556 Power Supply, 590A preamp and SCA, and 449 ratemeter).[63] The electronics allows for counting to absolute time intervals or for gating detectors according to the total number of counts in another detector (typically used to monitor the beam intensity immediately prior to the sample). Transistor–transistor logic signals from the CAMAC motor controllers are sent to motor drivers, which amplify the signals as appropriate for different motors (drivers from ACS,[64] 4-phase stepping motors from Superior Electric or Vexta). The software controls approximately 40 motors. An IEEE-488 interface board (National Instruments[65]) allows other signals to be recorded by the computer. These include signals from a multichannel buffer (Ortec 918 and 476-4 multiplexer[63]) that records the output of a linear detector (Ordela[46]) as well as any signals recorded by a scanner multimeter (Keithley Instruments model 199[66]) such as the resistance of thermistors (to measure sample temperatures).

VII. MEASUREMENTS

In this section, a few measurements are discussed, which illustrate the capabilities of the spectrometer.
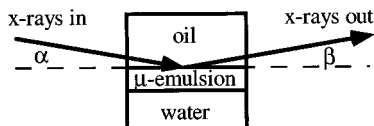
FIG. 7. Schematic of liquid–liquid scattering geometry.

A. Liquid–liquid interfacial structure

Liquid–liquid interfaces are model systems to study interfacial phenomena in a variety of technologically and scientifically important areas. Recent measurements at the oil–monolayer–water interface by Lee *et al.* and McClain *et al.* used neutron reflectivity and x-ray scattering, respectively, to probe the large interfacial roughness.[67,68]

At X19C, we are currently studying the oil–microemulsion interface in ternary liquid systems containing a straight-chain oil, water, and a surfactant from the homologous series C_iE_j [*n*-alkyl polyglycol ether $CH_3(CH_2)_{i-1}(OCH_2CH_2)_jOH$].[69–72] We have made x-ray scattering measurements from the oil–microemulsion interface of several ternary mixtures that include one of the surfactants, C_4E_1, C_6E_2, or $C_{10}E_4$. The mixtures using C_4E_1 or C_6E_2 yield qualitatively similar results. The mixtures with $C_{10}E_4$ have much rougher interfaces ($\sigma \geqslant 200$ Å) and will be discussed elsewhere. Here, we present studies of a C_4E_1–water–decane (1:1:3) mixture at 35.00 °C prepared in a vapor-tight sample cell. Under these conditions, the solution is in a three-phase state with a middle-phase microemulsion. The primary experimental challenge occurs because the x-ray beam fully traverses the diameter of one of the bulk phases. The concurrent absorption and bulk scattering determines the need for a small sample that, in turn, requires a very small x-ray beam (10 μm vertically). The high brilliance of a synchrotron x-ray source is needed to meet this experimental challenge.

We used H_2O from a Barnstead Nanopure UV system, decane (99+%) purchased from Sigma, and C_4E_1 (>99.8%) purchased from Fluka. The solution is contained in a polycarbonate sample cell of approximate cylindrical symmetry. The x rays pass in and out of the cell through two thin mylar windows attached to the body of the cell with Kalrez *o* rings. The sample cell is surrounded by a two-stage thermostat and temperature controlled to within 0.005 °C.

In this design, the x rays pass through 35 mm of the upper phase, necessitating the use of high energy x rays (see Fig. 7). The absorption length of the upper decane-rich phase (at 35 °C) at 15 keV is 15 mm, resulting in an absorption loss of 90%. By using a multilayer monochromator crystal at the X19C surface spectrometer, we have adequate intensity to perform these experiments (6×10^{11} photons/s at 15 keV in a 0.5 mm×1 mm spot).

The reflectivity data (from the oil–microemulsion interface) shown in Fig. 8 are very near Q_c and cannot be analyzed with the Born approximation given in Eqs. (3) and (4). Instead, these data were analyzed with the distorted wave Born approximation to determine the interfacial roughness, σ, using the result given by[32,68,73]
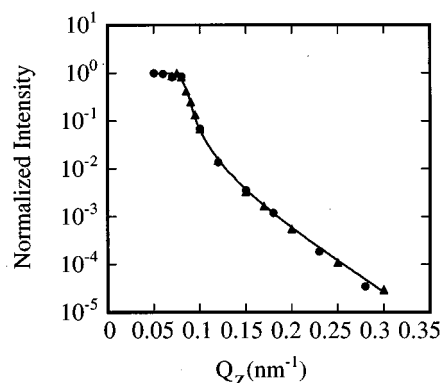

FIG. 8. Reflected intensity versus Q_z for x rays reflected from the oil–microemulsion interface of a C_4E_1–decane–water mixture. The two symbols (circles and triangles) represent two different data sets from two different samples measured during two different experimental runs. The solid line is a fit to Eq. (21).

$$\frac{R(Q_z)}{I_o} \cong \left| \frac{Q_z - Q_z^T}{Q_z + Q_z^T} \right|^2 \exp(-\sigma^2 Q_z Q_z^T), \qquad (21)$$

where $R(Q_z)$ is the reflected intensity as a function of the wave-vector Q_z normal to the interface, I_o is the incident intensity, and $Q_z^T \cong \sqrt{Q_z^2 - Q_c^2}$ is the z component of wave-vector transfer with respect to the microemulsion phase. The solid line in Fig. 8 is a fit to Eq. (21) that yields $\sigma = 66$ Å ± 3 Å. This value is much larger than the largest molecular size (~ 10 Å), and is indicative of a strongly fluctuating interface.

Figure 9 shows the surface diffuse scattering measured as a function of β for fixed α. The larger peak occurs at the specular condition ($\alpha = \beta$); the smaller peak occurs at the critical angle, α_c, and is due to the enhanced surface scattering from surface fluctuations. The solid line results from fitting to the form given by Eq. (8) using the surface roughness determined by the specular reflectivity. The one significant fitting parameter is the interfacial tension, $\gamma = 0.18 \pm 0.01$ dyn/cm. In addition to the interfacial tension, a linearly sloped background on the order of 10% of the peak heights is fit. We have also fit our data to a slightly less
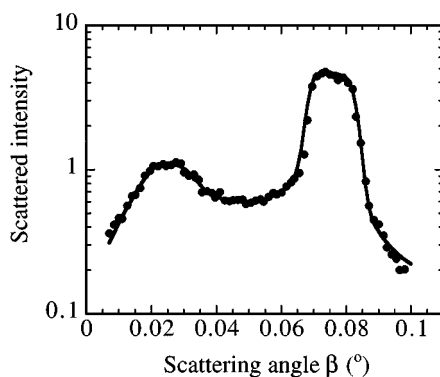

FIG. 9. Intensity of the surface diffuse scattering at fixed incident angle, $\alpha = 0.068°$, plotted as a function of the scattering angle, β. The solid line is a fit to Eq. (8).

approximate form for the distorted wave Born approximation as given by Sinha *et al.*[32] There are slight quantitative differences, however, the qualitative features remain the same.

The data in Figs. 8 and 9 are fit simultaneously because of a small interplay between the roughness value needed to fit the reflectivity and that needed to fit the diffuse scattering. This occurs because some diffusely scattered x rays are measured by the detector set for the specular condition. To extract the value for the roughness consistent simultaneously with both reflectivity and diffuse scattering requires subtracting the diffuse scattering from the specular measurements during the fitting process. This will be discussed elsewhere.[21]

B. Thermal expansion coefficient of a perfluorinated monolayer at the air–water interface

Grazing incidence x-ray diffraction measurements of a monolayer of perfluoro-*n*-eicosane $[F(CF_2)_{20}F]$ at the water surface were made at X19C. Although this molecule is not a surfactant in the traditional sense of having both hydrophilic and hydrophobic moieties, nevertheless, it forms well-ordered monolayers supported on water. It is plausible that a delicate balance between a strongly attractive lateral fluorocarbon–fluorocarbon interaction and the weaker van der Waals forces between the fluorocarbon molecules and the water allows the fluorocarbon molecules to spread over the surface as a single layer. Due to the unusual nature of this monolayer, it is sensible to ask if it shows some of the characteristic features of bulk fluorocarbons. For example, an earlier study of this monolayer had indicated that it might show evidence for a structural transition similar to that seen for Teflon. However, our study of the thermal expansion coefficient over the temperature range from 2 to 35 °C precludes this possibility.[17]

Monolayers of perfluoro-*n*-eicosane spread onto a pure water surface form a hexagonal phase with the molecules oriented perpendicular to the surface. The studies discussed here were measured on monolayers where the macroscopic areal density varied from 0.45 to 0.50 nm^2 per molecule. The molecules form ordered monolayer patches whose unit cell is constant over the macroscopic density range studied here.

The data shown in Fig. 10 demonstrate the temperature dependence of the (0,1) diffraction peaks of three separate monolayers of perfluoro-*n*-eicosane in the hexagonal phase. The average thermal expansion coefficient of the chain–chain separation computed from this data is $(7.1 \pm 0.8) \times 10^{-5}$ nm/°C. Although we have not found any studies of the thermal expansion of bulk fluoroalkanes, this value is similar to thermal expansion coefficients of bulk alkanes (6×10^{-5} nm/°C) in the tightly packed low-temperature orthorhombic phase. However, the hexagonal (rotator) phase of bulk alkanes is more loosely packed and has a much greater thermal expansion, of the order of 5×10^{-4} nm/°C.

The three sets of data shown in Fig. 10 illustrate the repeatability of the spectrometer. Data sets B and C were taken during a single trip to the synchrotron (NSLS). Slight realignment of the spectrometer between the spreading of these two monolayers did not affect these indistinguishable data sets. However, data set A was measured during a different trip to the synchrotron and is offset from B and C by
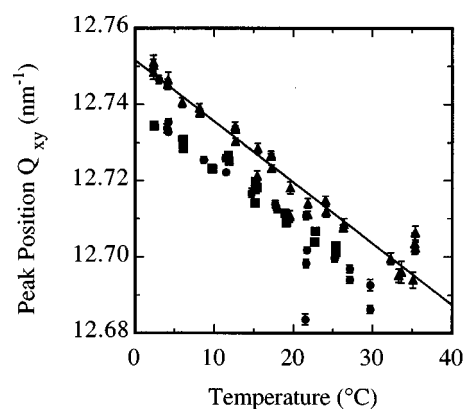
FIG. 10. Diffraction peak center Q_{xy} as a function of the substrate water temperature. Data are shown for three separately prepared monolayers. Circular and square symbols represent data taken during the same experimental run; the triangles refer to data taken during a different experimental run. The line is a least-squares linear fit to the data represented by the triangles.

0.015 nm^{-1} in Q_{xy}. The complete alignment of the spectrometer, including the beamline mirror, is responsible for this systematic error in Q_{xy}. Note that the thermal expansion, indicated by the slope of the data, is essentially the same for all three data sets.

APPENDIX: ENERGY ERROR DUE TO ALIGNMENT

Although most of the techniques we intend to use can accommodate the small energy changes that occur as χ is changed, the measurement of differential anomalous reflectivity requires a very constant incident energy for all incident angles. It can be shown that if the incoming beam is misaligned from the χ axis by an angle ϵ in the vertical and an angle δ in the horizontal (see Fig. 11), then the change in the angle Φ required to reorient the monochromator crystal for Bragg reflection at a particular energy is $\Delta\Phi \sim \epsilon\chi - (1/2)\delta\chi^2$. To see this, write $\mathbf{k}_{in,m}$ in (ξ,η,ζ) space including the effect of ϵ and δ (see Fig. 12),
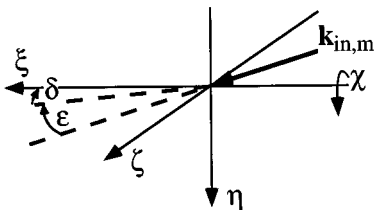
FIG. 11. Illustration of misalignment between $\mathbf{k}_{in,m}$ and the χ axis (collinear with the ξ axis). The angular deviation in the horizontal is δ; the deviation in the vertical is ϵ.

$$\mathbf{k}_{in,m} = k(\cos(\epsilon)\cos(\delta), \sin(\epsilon), \cos(\epsilon)\sin(\delta)). \qquad (A1)$$

For $\chi = 0$, the reciprocal lattice vector can be written as

$$\boldsymbol{\tau} = \tau(-\cos(\pi/2 - \theta_B - \delta), 0, \sin(\pi/2 - \theta_B - \delta)). \qquad (A2)$$

Using the Bragg condition, $-2\boldsymbol{\tau} \cdot \mathbf{k} = \tau^2$, it is easily found that $\tau^2 = 2k\tau\cos(\epsilon)\sin(\theta_B)$ or $\tau/2k = \sin(\theta_B)$ to first order in ϵ.

By considering the projection of τ into the ξ–ζ plane for $\chi \neq 0$, it is seen that the ξ component of τ is independent of χ (Fig. 12). This allows us to write, for $\chi \neq 0$,

$$\boldsymbol{\tau} = \tau(-\cos(\pi/2 - \theta_B - \delta), \cos(\theta_B + \delta)\sin(\chi),$$
$$\times \cos(\theta_B + \delta)\cos(\chi)). \qquad (A3)$$

Using the Bragg condition, Eq. (A3) leads to

$$\frac{\tau}{2k} \cong \sin(\theta_B) - \epsilon\chi + \delta\chi^2/2, \qquad (A4)$$

to first order in δ and ϵ. The first term is the usual Bragg condition. The remaining two terms yield the deviation from the Bragg condition that we wanted to calculate.

Correct alignment of both the 3-circle Θ axis (to set δ equal to zero) and the tilt of the monochromator tank (to set ϵ equal to zero) can be used to maintain constant energy as a function of incident angle. This alignment proceeds as follows: Once the beam is adjusted to go through the center of the 3-circle, two adjustments must be made to align the beam horizontally (δ) and vertically (ϵ). Both alignments are carried out by rotating the monochromator crystal, using the Φ stage, to be parallel to the beam for two values of χ that vary 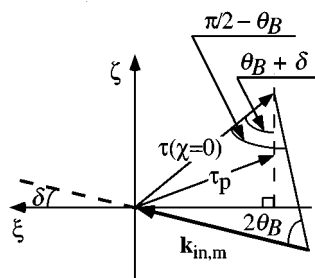by 180°. To determine if the monochromator crystal is parallel to the beam, the crystal is placed into the beam and Φ is rocked. As long as the crystal is well within the beam, then the peak in the intensity will have a maximum that corresponds to the crystal being parallel to the beam. If the two Φ values required for parallelism are different, then a correction of half the difference is made. To adjust δ, the two χ positions used are $+/-90°$ and the correction is made by a Θ motion (3-circle Θ stage). To adjust ϵ, the two χ positions used are 0° and 180° and the correction is made by the kinematic mount on the monochromator tank.

A typical alignment of the spectrometer is capable of reducing $\Delta E/E$ to less than 5 eV over the full range of reflection angles without too much difficulty. Given the other limitations in energy resolution at X19C, this resolution is adequate.

FIG. 12. Projection into the ξ–ζ plane of the monochromator reflection kinematics when a misalignment exists between $\mathbf{k}_{in,m}$ and the χ axis (collinear with the ξ axis) as illustrated in Fig. 11.

[1] D. Sluis and S. A. Rice, J. Chem. Phys. **79**, 5658 (1983).
[2] L. Bosio and M. Oumezine, J. Chem. Phys. **80**, 959 (1984).
[3] A. H. Weiss, M. Deutsch, A. Braslau, B. M. Ocko, and P. S. Pershan, Rev. Sci. Instrum. **57**, 2554 (1986).
[4] J. Als-Nielsen, F. Christensen, and P. S. Pershan, Phys. Rev. Lett. **48**, 1107 (1982).
[5] J. Als-Nielsen and P. S. Pershan, Nucl. Instrum. Methods Phys. Res. **208**, 545 (1983).
[6] P. S. Pershan, A. Braslau, A. H. Weiss, and J. Als-Nielsen, Phys. Rev. A **35**, 4800 (1987).
[7] P. S. Pershan, J. Phys. (Paris), Colloq. **50**, C7 (1989).
[8] D. K. Schwartz, M. L. Schlossman, and P. S. Pershan, J. Chem. Phys. **96**, 2356 (1992).
[9] S. W. Barton, B. N. Thomas, E. B. Flom, S. A. Rice, B. Lin, J. B. Peng, J. B. Ketterson, and P. Dutta, J. Chem. Phys. **89**, 2257 (1988).
[10] B. Lin, Ph.D. thesis (Northwestern University, 1990).
[11] K. M. Robinson and J. A. Mann, J. Phys. Chem. **95**, 2456 (1991).
[12] B. R. McClain, Ph.D. thesis (M.I.T., 1994).
[13] L. Bosio, R. Cortes, G. Folcher, and M. Oumezine, Rev. Phys. Appl. **20**, 437 (1985).
[14] J. Penfold and R. K. Thomas, J. Phys.: Condens. Matter **2**, 1369 (1990).
[15] Y. R. Shen, Annu. Rev. Phys. Chem. **40**, 327 (1989).
[16] K. B. Eisenthal, Annu. Rev. Phys. Chem. **43**, 627 (1992).
[17] Z. Huang, M. L. Schlossman, A. A. Acero, Z. Zhang, N. Lei, and S. A. Rice, Langmuir **11**, 2742 (1995).
[18] Z. Huang, A. A. Acero, N. Lei, S. A. Rice, Z. Zhang, and M. L. Schlossman, J. Chem. Soc. Faraday Trans. **92**, 545 (1996).
[19] N. Lei, Z. Huang, and S. A. Rice, J. Chem. Phys. **104**, 4802 (1996).
[20] S. M. Williams, Z. Zhang, D. Mitrinovic, and M. L. Schlossman, Bull. Am. Phys. Soc. **41**, 174 (1996).
[21] S. M. Williams, Z. Zhang, D. Mitrinovic, Z. Huang, and M. L. Schlossman (unpublished).
[22] B. Lin, M. L. Schlossman, M. Meron, Z. Huang, P. J. Viccaro, S. M. Williams, T. Morkved, and H. Jaeger (unpublished).
[23] B. Lin, M. L. Schlossman, M. Meron, S. M. Williams, and P. J. Viccaro, Rev. Sci. Instrum. **67**, 1 (1996).
[24] P. S. Pershan, Faraday Discuss. Chem. Soc. **89**, 231 (1990).
[25] J. Als-Nielsen, D. Jacquemain, K. Kjaer, F. Leveiller, M. Lahav, and L. Leiserowitz, Phys. Rep. **246**, 251 (1994).
[26] S. Dietrich and A. Haase, Phys. Rep. **260**, 1 (1995).
[27] M. L. Schlossman and P. S. Pershan, in *Light Scattering by Liquid Surfaces and Complementary Techniques*, edited by D. Langevin (Marcel Dekker, New York, 1992), p. 365.
[28] J. Als-Nielsen and K. Kjaer, in *Phase Transitions in Soft Condensed Matter*, edited by T. Riste and D. Sherrington (Plenum, New York, 1989), p. 145.
[29] M. L. Schlossman, in *Encyclopedia of Applied Physics*, edited by G. L. Trigg (VCH, New York, 1997), Vol. 20, p. 311.
[30] M. Born and E. Wolf, *Principles of Optics* (Pergamon, Oxford, 1980).
[31] L. G. Parratt, Phys. Rev. **95**, 359 (1954).
[32] S. K. Sinha, E. B. Sirota, S. Garoff, and H. B. Stanley, Phys. Rev. B **38**, 2297 (1988).
[33] F. P. Buff, R. A. Lovett, and F. H. Stillinger, Phys. Rev. Lett. **15**, 621 (1965).

[34] O. M. Magnussen, B. M. Ocko, M. J. Regan, K. Penanen, P. S. Pershan, and M. Deutsch, Phys. Rev. Lett. **74**, 4444 (1995).

[35] M. J. Regan, E. H. Kawamoto, S. Lee, P. S. Pershan, N. Maskil, M. Deutsch, O. M. Magnussen, and B. M. Ocko, Phys. Rev. Lett. **75**, 2498 (1995).

[36] S. Dietrich and H. Wagner, Z. Phys. B **56**, 207 (1984).

[37] D. K. Schwartz, M. L. Schlossman, E. H. Kawamoto, G. J. Kellogg, P. S. Pershan, and B. M. Ocko, Phys. Rev. A **41**, 5687 (1990).

[38] A. Braslau, P. S. Pershan, G. Swislow, B. M. Ocko, and J. Als-Nielsen, Phys. Rev. A **38**, 2457 (1988).

[39] R. S. Becker, J. A. Golovchenko, and J. R. Patel, Phys. Rev. Lett. **50**, 153 (1983).

[40] S. Dietrich and H. Wagner, Z. Phys. B **59**, 35 (1985).

[41] H. Dosch, Phys. Rev. B **35**, 2137 (1987).

[42] H. Dosch, B. W. Batterman, and D. C. Wack, Phys. Rev. Lett. **56**, 1144 (1986).

[43] R. Feidenhans'l, Surf. Sci. Rep. **10**, 105 (1989).

[44] W. C. Marra, P. Eisenberger, and A. Y. Cho, J. Appl. Phys. **50**, 6927 (1979).

[45] A. Zangwill, *Physics at Surfaces* (Cambridge University Press, Cambridge, 1988).

[46] Ordela, Oak Ridge Detector Laboratory, Inc., 139 Valley Court, Oak Ridge, Tennessee 37830.

[47] M. Stamm, G. Reiter, and S. Huttenbach, Physica B **156&157**, 564 (1989).

[48] J. Penfold, J. Phys. (Paris), Colloq. **50**, C7 (1989).

[49] G. P. Felcher, R. O. Hilleke, R. K. Crawford, J. Haumann, R. Kleb, and G. Ostrowski, Rev. Sci. Instrum. **58**, 609 (1987).

[50] J. M. Bloch and P. Eisenberger, Nucl. Instrum. Methods Phys. Res. B **31**, 468 (1988).

[51] Osmic, Inc., 1788 Northwood Drive, Troy, MI 48084.

[52] N. Lei, Z. Huang, and S. A. Rice (unpublished).

[53] Huber Diffraktionstechnik GmBH, D-8219 Rimsting, Germany.

[54] Blake Industries, Inc., 660 Jerusalem Road, NJ 07076.

[55] Dover Instrument Corp., 200 Flanders Road, P. O. Box 200, Westboro, MA 01581.

[56] Newport Research Corp., 1791 Deere Avenue, Irvine, CA 92714.

[57] JRS, J. R. Sandercock, Zwillikerstrasse 8, CH-8910 Affoltern a.A., Switzerland.

[58] Heidenhain Corp., 115 Commerce Dr., Schaumburg, IL 60173.

[59] Certified Scientific Software, P. O. Box 640, Cambridge, Massachusetts 02139.

[60] DSP Technology Inc., 48500 Kato Road, Fremont, CA 94538-7338.

[61] Bicron Corp., 12345 Kinsman Road, Newbury, OH 44065-9677.

[62] Kinetic Systems Corp., 11 Maryknoll Drive, Lockport, IL 60441.

[63] EG&G Ortec, 100 Midland Road, Oak Ridge, TN 37831-0895.

[64] Advanced Control Systems Corp., Old Mine Rock Road, Hingham, MA 02043.

[65] National Instruments, 6504 Bridge Point Parkway, Austin, TX 78730–5039.

[66] Keithley Instruments, 28775 Aurora Road, Cleveland, Ohio 44139.

[67] L. T. Lee, D. Langevin, and B. Farnoux, Phys. Rev. Lett. **67**, 2678 (1991).

[68] B. R. McClain, D. D. Lee, B. L. Carvalho, S. G. J. Mochrie, S. H. Chen, and J. D. Litster, Phys. Rev. Lett. **72**, 246 (1994).

[69] M. Kahlweit and R. Strey, Angew. Chem. Int. Ed. Engl. **24**, 654 (1985).

[70] M. Kahlweit and R. Strey, J. Phys. Chem. **90**, 5239 (1986).

[71] M. Kahlweit and R. Strey, J. Phys. Chem. **91**, 1553 (1987).

[72] M. Kahlweit, R. Strey, D. Haase, H. Kunieda, T. Schmeling, B. Faulhaber, M. Borkovec, H.-F. Eicke, G. Busse, F. Eggers, T. Funck, H. Richmann, L. Magid, O. Söderman, P. Stilbs, J. Winkler, A. Dittrich, and W. Jahn, J. Colloid Interface Sci. **118**, 436 (1987).

[73] L. Nevot and P. Croce, Rev. Phys. Appl. **15**, 761 (1980).